Energy Materials and Devices

Open Access
Research Article

Graphical Abstract

Thermal activation of graphitic carbon nanosheets for high-performance oxygen electrocatalysis

Yongqi Chen[1,2,†], Zongheng Cen[2,†], Junlong Huang[3] ✉, Tan Yi[2], Min Liang[2], Yiwei Ji[2], Ming Liu[1] ✉, and Shaohong Liu[2] ✉

[1] *Shenzhen All-Solid-State Lithium Battery Electrolyte Engineering Research Center, Institute of Materials Research (IMR), Tsinghua Shenzhen International Graduate School, Shenzhen 518055, China*
[2] *Key Laboratory for Polymeric Composite and Functional Materials of Ministry of Education, School of Chemistry, Sun Yat-sen University, Guangzhou 510006, China*
[3] *Advanced Institute for Materials Research (WPI-AIMR), Tohoku University, Sendai 980-8577, Japan*

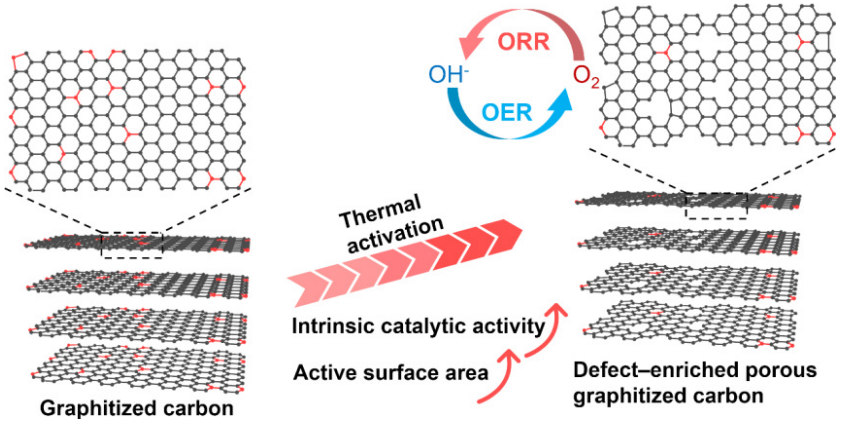

An efficient strategy has been demonstrated for the activation of low-active graphitized carbon nanosheets through a thermal-driven nitrogen atom removal process. The resulting defect-enriched porous graphitized carbon nanosheets simultaneously combine abundant highly active intrinsic defects with a high graphitization degree and numerous micro/mesopores, providing excellent activity as bifunctional electrocatalysts for oxygen reduction reaction (ORR) and oxygen evolution reaction (OER).

✉ Address correspondence to
Junlong Huang, huang.junlong.d5@tohoku.ac.jp;
Ming Liu, liuming@sz.tsinghua.edu.cn;
Shaohong Liu, liushh27@mail.sysu.edu.cn

Received: November 17, 2025
Revised: December 30, 2025
Accepted: January 4, 2026

Read Online

Citation: Chen Y., Cen Z., Huang J., et al. Thermal activation of graphitic carbon nanosheets for high-performance oxygen electrocatalysis. *Energy Mater. Devices*, 2026, 4(1), 9370084. https://doi.org/10.26599/EMD.2026.9370084

Open Access This article is licensed under a Creative Commons Attribution 4.0 International License (CC BY 4.0), which permits reusers to distribute, remix, adapt, and build upon the material in any medium or format, so long as attribution is given to the original author(s) and the source, a link to the license is provided, and any changes made are indicated. See https://creativecommons.org/licenses/by/4.0/

© The author(s) 2026. Published by Tsinghua University Press.

Energy Materials and Devices
https://doi.org/10.26599/EMD.2026.9370084
Open Access
Research Article

Thermal activation of graphitic carbon nanosheets for high-performance oxygen electrocatalysis

Yongqi Chen[1,2,†], Zongheng Cen[2,†], Junlong Huang[3] ✉, Tan Yi[2], Min Liang[2], Yiwei Ji[2], Ming Liu[1] ✉, and Shaohong Liu[2] ✉

[1] *Shenzhen All-Solid-State Lithium Battery Electrolyte Engineering Research Center, Institute of Materials Research (IMR), Tsinghua Shenzhen International Graduate School, Shenzhen 518055, China*
[2] *Key Laboratory for Polymeric Composite and Functional Materials of Ministry of Education, School of Chemistry, Sun Yat-sen University, Guangzhou 510006, China*
[3] *Advanced Institute for Materials Research (WPI-AIMR), Tohoku University, Sendai 980-8577, Japan*
[†] *Yongqi Chen and Zongheng Cen contributed equally to this work.*

Cite this article: *Energy Mater. Devices* 2026, **4**(1): 9370084. https://doi.org/10.26599/EMD.2026.9370084

ABSTRACT

Carbon-based electrocatalysts have considerable potential for application in renewable and clean energy conversion systems. Although graphitic carbons have the advantages of high conductivity and electrolyte corrosion resistance, their sp2-hybridized skeleton often leads to poor porosity and insufficient intrinsic active sites, resulting in suboptimal catalytic activity for sluggish multi-electron redox reactions. Herein, we demonstrate an efficient strategy for the activation of low-active graphitized carbon nanosheets by a thermal-driven nitrogen atom removal process. The elimination of nitrogen atoms at high temperatures facilitates the rearrangement of neighboring carbon atoms, leading to numerous carbon defects and an increased surface area, while retaining the long-range ordered graphitic structure. As a result, the as-obtained defect-enriched porous graphitized carbon nanosheets (DPGCNSs) simultaneously combine abundant highly active intrinsic defects with a high graphitization degree and numerous micro/mesopores, demonstrating low overpotential and favorable kinetics for oxygen reduction and oxygen evolution reactions. Remarkably, rechargeable Zn–air batteries with DPGCNSs catalysts demonstrate superior cycling performance, exceeding 700 cycles with no obvious voltage fading.

KEYWORDS

graphitic carbon, carbon defect, thermal activating, oxygen electrocatalysis, Zn–air battery

1 Introduction

With rapidly increasing energy demand and growing environmental concerns, significant efforts have been devoted to developing renewable and clean energy conversion technologies. Among these, electrochemical energy conversion systems—such as hydrogen fuel cells, metal–air batteries, and water-splitting devices—have emerged as highly promising and environmentally friendly strategies for achieving carbon neutrality[1,2]. However, the performance of these devices is largely constrained by sluggish electrochemical redox reactions—including the hydrogen evolution reaction, oxygen evolution reaction (OER), and oxygen reduction reaction (ORR)—which involve multiple interfacial processes and multi-electron transfers[3]. Electrocatalysts are therefore essential to lower kinetic barriers and enhance energy conversion efficiency. Although traditional noble metal-based materials (e.g., platinum, palladium, and iridium-based catalysts) remain the most efficient for these reactions, their high cost, limited availability, and poor long-term stability significantly hinder widespread application[4–6]. Consequently, there is a pressing need to develop next-generation, non-noble metal-based electrocatalysts that can deliver comparable performance at reduced cost.

Carbon-based electrocatalysts have attracted extensive attention due to their low cost, excellent electrical conductivity, chemical stability, and tunable structures[7–11]. To achieve both high catalytic activity and long operational lifetime, an optimized carbon-based electrocatalyst should satisfy three criteria: (i) abundant intrinsic active sites to facilitate reactant adsorption and reduce multi-step reaction barriers, (ii) a highly graphitic framework to accelerate electron transfer and maintain electrolyte tolerance, and (iii) a porous structure to promote mass transport and maximize site accessibility. Recent studies have explored atomic metal-decorated carbon catalysts, which exhibit enhanced catalytic activity owing to their high atom

Received: November 17, 2025 / **Revised:** December 30, 2025 / **Accepted:** January 4, 2026

✉**Address correspondence to** Junlong Huang, huang.junlong.d5@tohoku.ac.jp; Ming Liu, liuming@sz.tsinghua.edu.cn; Shaohong Liu, liushh27@mail.sysu.edu.cn

utilization efficiency[12–15]. However, the amorphous nature of the carbon matrix and the high surface energy of atomic metal sites often lead to structural instability and rapid performance decay. In contrast, graphitic carbon materials—including carbon nanotubes, onion-like carbon, and few-layered graphene—possess a predominantly sp^2-hybridized skeleton, providing high structural stability and excellent resistance to electrolyte corrosion[16–18]. Unfortunately, the intrinsic active sites in graphitic carbon are limited, and the low porosity further restricts catalytic accessibility, resulting in suboptimal activity for multi-electron redox reactions. Thus, introducing a high density of catalytic sites and nanopores into graphitic carbon, while preserving its long-range conjugated structure, remains a fundamental yet challenging goal for achieving highly efficient electrocatalytic performance.

Herein, we report an efficient strategy for the preparation of defect-enriched porous graphitized carbon nanosheets (DPGCNSs), which exhibit abundant intrinsic defects, a high degree of graphitization, and numerous micro/mesopores. This strategy involves the preparation of nitrogen-doped graphitized carbon nanosheets (NGCNSs) via active-template catalytic pyrolysis at a relatively low temperature (e.g., 800°C), followed by the removal of the doped N atoms at a higher temperature (e.g., 1075°C). Notably, the elimination of N atoms triggers the rearrangement of neighbor C atoms, leading to the formation of carbon defects and an increased surface area, while effectively retaining the long-range ordered graphitic structure. Benefiting from the unusually integrated merits of sufficient intrinsic defects with favorable catalytic activity, a highly graphitic skeleton with excellent electrical conductivity, and a 2D porous structure enabling efficient mass transport, the as-constructed DPGCNSs demonstrate high activity as bifunctional electrocatalysts for ORR and OER, exhibiting low overpotential and favorable kinetics. Moreover, the DPGCNSs also display superior performance as cathode materials in primary and rechargeable Zn–air batteries, demonstrating significant potential for practical application.

2 Materials and methods

2.1 Synthesis of DPGCNSs

Typically, aniline and $FeCl_3{\cdot}6H_2O$ with a molar ratio of 1:5 were initially mixed at 60°C for 1 h, followed by aging at room temperature for 1 h. The as-obtained poly(aniline) (PANI) and $FeCl_3{\cdot}6H_2O$ mixture was then thermally pyrolyzed under flowing N_2 at 800°C and 1000°C for 3 h with a heating rate of 5°C min^{-1}, followed by etching with 6 mol L^{-1} HCl, giving rise to NGCNSs. Afterward, NGCNSs were further heated at 1075°C for 1 h, leading to the formation of DPGCNSs. Tailoring the active-template catalytic pyrolysis temperature (e.g., 600–1000°C) and N-removal temperature (e.g., 1000–1150°C) can generate carbon products with different lattice structures and defect densities. By changing the precursor and following the same preparation process, a series of defect-poor graphitized carbon materials (GCMs) samples were obtained. The detailed preparation procedure and corresponding material characterization can be found in the Supplementary Materials.

2.2 Electrochemical measurements

All electrochemical tests were conducted in a three-electrode cell at room temperature and recorded on a CHI660E electrochemical workstation (Shanghai Chenhua Instruments Co., Ltd., China). Ag/AgCl and platinum plate electrodes were used as the reference and counter electrodes, respectively. A rotating disk electrode (RDE) with a 0.196 cm^2 glassy carbon disk was used as the working electrode to evaluate the catalytic activity toward the ORR. A rotating ring-disk electrode (RRDE) with a Pt ring (6.5 mm inner diameter and 8.5 mm outer diameter) and a glassy carbon disk (5.5 mm diameter) was used as the working electrode to characterize the catalytic selectivity of different electrocatalysts. The electrochemical experiments were carried out in O_2 saturated electrolytes with 0.1 mol L^{-1} KOH for ORR and 1 mol L^{-1} KOH for OER, respectively. Linear sweep voltammetry (LSV) was performed at a scan rate of 10 mV s^{-1}. Further details on the procedures for electrochemical measurements and Zn–air battery tests are provided in the Supplementary Materials.

3 Results and discussion

In this approach, aniline is chosen as the precursor owing to its high carbonizability and considerable N content, and $FeCl_3{\cdot}6H_2O$ is employed as the 2D active salt template. Initially, aniline is mixed with molten $FeCl_3{\cdot}6H_2O$ and undergoes oxidative polymerization to yield polyaniline, as evidenced by Fourier transform infrared (FTIR) spectra (Fig. S1 in Supplementary Materials). Afterward, the mixture of polyaniline and $FeCl_3{\cdot}6H_2O$ salt is pyrolyzed at 800°C under a flowing inert atmosphere, followed by the removal of the residual iron species, leading to the formation of NGCNSs. Scanning electron microscopy (SEM) images reveal a 2D sheet-like morphology of NGCNSs (Fig. 1a), which can be attributed to the template effect of $FeCl_3{\cdot}6H_2O$[19]. X-ray photoelectron spectroscopy (XPS) spectrum reveals the presence of N in NGCNSs (Fig. S2a in Supplementary Materials), and the nitrogen species can be resolved into four peaks at 398.3, 399.6, 400.8, and 403.0 eV (Fig. S2b in Supplementary Materials), corresponding to pyridinic N (N6), pyrrolic N (N5), graphitic N (NQ), and oxidized N (NO), respectively[20–22]. The as-obtained NGCNSs are further heated at higher temperatures (i.e., 1075°C) to remove relatively unstable N species from carbon skeleton (mainly N6 and N5), giving rise to DPGCNSs with a decreased total N content (1.6 wt% for DPGCNSs vs. 2.3 wt% for NGCNSs). Owing to the very low residual Fe content in NGCNSs (0.167 wt%) and DPGCNSs (0.174 wt%), as determined by inductively coupled plasma–mass spectrometry, no obvious Fe signals were observed in the high-resolution Fe 2p XPS spectra (Fig. S3 in Supplementary Materials). The corresponding energy dispersive spectroscopy further confirms that the characteristic signals of Fe are absent, with no apparent Fe aggregation observed in the elemental mapping (Fig. S4 in Supplementary Materials)[23]. As shown in Fig. 1b, the resultant DPGCNSs retain the 2D nanostructure of NGCNSs. High-resolution transmission electron micro-

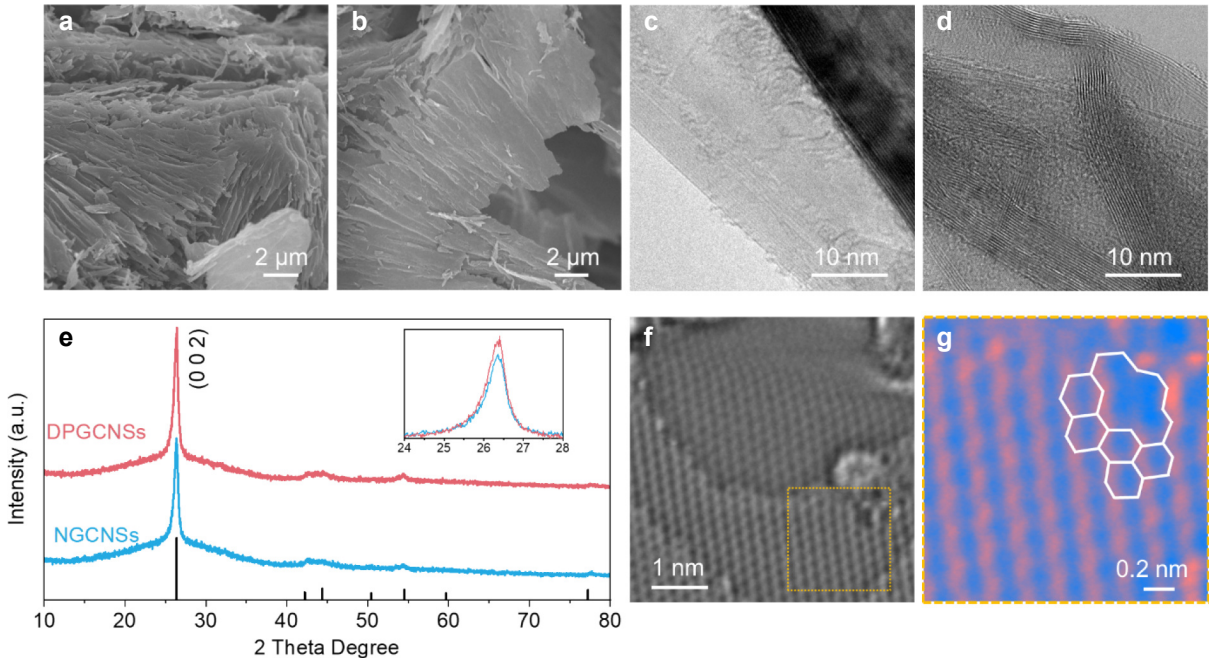

Figure 1 SEM images of NGCNSs (a) and DPGCNSs (b). HRTEM images of NGCNSs (c) and DPGCNSs (d). (e) XRD patterns of DPGCNSs and NGCNSs. (f) Aberration-corrected high-angle-annular-dark-field scanning transmission electron microscopy (AC HAADF-STEM) image of DPGCNSs. (g) Expanded image of the dotted box in (f), presenting the existence of vacancies and common hexagonal rings.

scopy (HRTEM) images show that both NGCNSs and DPGCNSs exhibit well-defined graphitic structures with long-range ordered carbon layers, suggesting a high graphitization degree (Figs. 1c and 1d). The structural characteristics of DPGCNSs are further analyzed by X-ray diffraction (XRD). As shown in Fig. 1e, a sharp (002) peak at 26.4° is observed for DPGCNSs, indicating a highly graphitic structure, which is consistent with the HRTEM observations. According to the Bragg equation, the average lattice spacing (d_{002}) of DPGCNSs is calculated to be 0.3373 nm, and the related graphitization index (g_p) reaches 0.78, close to those of NGCNSs (d_{002} = 0.3378 nm, g_p = 0.72). These indicate that the carbon skeleton retains a graphitic structure after N removal at high temperatures. Accordingly, the electrical conductivity of DPGCNSs (4.673 S cm^{-1}) is comparable to that of NGCNSs (4.717 S cm^{-1}). It has been demonstrated that the elimination of N atoms can lead to the rearrangement of neighboring carbon atoms and simultaneously produce intrinsic carbon defects[24–26]. As expected, AC-HRTEM and the corresponding filtered images reveal various carbon defects (e.g., edge defects and vacancies) as well as regular hexagons directly observable in the atomic structure of DPGCNSs (Figs. 1f and 1g).

Further in-depth characterizations were conducted to investigate the intrinsic carbon defects in DPGCNSs. According to the Raman spectrum of DPGCNSs in Fig. 2a, the D band (~1360 cm^{-1}), related to the disordered defective carbon constructure (e.g., edge defects, in-plane topological defects, and sp^3-hybridized defects) and G band (~1580 cm^{-1}), associated with the sp^2-hybridized graphitic carbon constructure are observed for DPGCNSs[27,28]. The intensity ratio of the D band area to the G band area (I_D/I_G) for DPGCNSs (1.20) is larger than that of NGCNSs (0.74), suggesting a higher degree of lattice disorder. The electron paramagnetic resonance (EPR) technique was further used to analyze the defect sites within carbon skeletons (Fig. 2b). Sharp peaks at g = 1.998 are observed for NGCNSs and DPGCNSs, which are associated with the unpaired electrons on π-conjugated carbon atoms[29,30]. DPGCNSs demonstrates a much higher intensity of EPR signal than NGCNSs, confirming that abundant intrinsic defects are generated in the carbon skeleton after the elimination of N atoms at high temperatures. N_2 adsorption–desorption measurements demonstrate that DPGCNSs deliver a type IV isotherm with an uptake at low relative pressure and an obvious hysteresis loop, indicating the presence of micropores and mesopores (Fig. 2c). Notably, compared with NGCNSs, DPGCNSs deliver an increased Brunauer–Emmett–Teller (BET) surface area (S_{BET}) (171 m^2 g^{-1} for DPGCNSs vs. 109 m^2 g^{-1} for NGCNSs) (Fig. 2d). These results indicate that the N-removal process at high temperatures might lead to the growth of pore structures, which is highly related to rich edge defects. The pyrolysis process from NGCNSs to DPGCNSs is further revealed by simultaneous thermal analyzer coupled with Fourier transform infrared spectrometry (STA-FTIR) measurements (Fig. 2e). Thermogravimetric curve shows that the NGCNSs display weight loss ranging from 800 to 1200°C. During this process, *in situ* infrared spectra indicate that the N-doping atoms release in the form of NH_3 (1400–1800 cm^{-1}); meanwhile, rearrangement of carbon atoms results in persistent volatilization of CO_2 (2150–2420 cm^{-1}), CO (double peaks between 2040–2200 cm^{-1}), and CH_4 (1600–1800 cm^{-1})[31]. Based on the above discussion, a schematic illustration is proposed to summarize the structural evolution from NGCNSs to DPGCNSs (Fig. 2f), where the removal of N-doping atoms, accompanied by the rearrangement of carbon atoms, generates intrinsic defects in the carbon lattice and

清華大學出版社 Tsinghua University Press | SciOpen

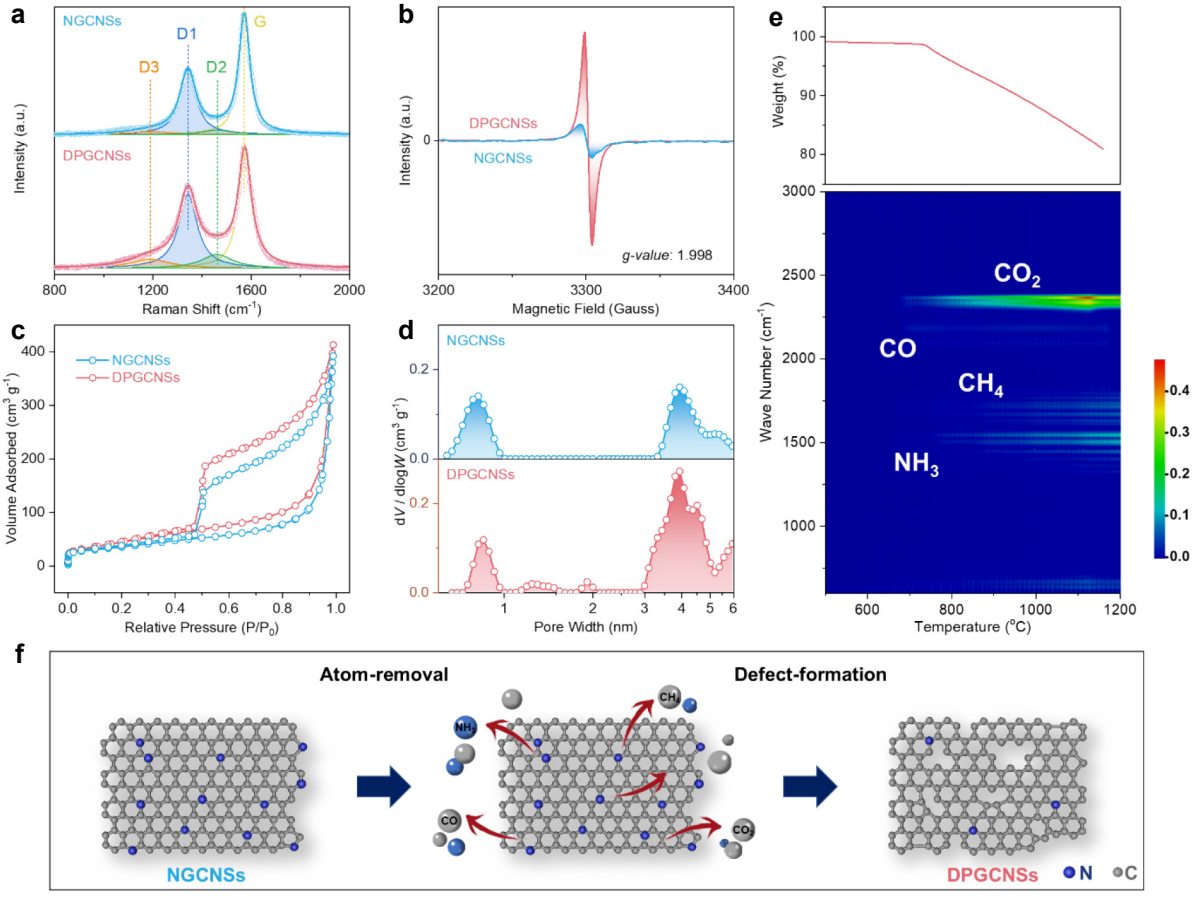

Figure 2 Raman spectra (a), EPR spectra (b), N_2 adsorption–desorption isotherms (c), and pore size distribution curves (d) of DPGCNSs and NGCNSs. (e) *In situ* STA-FTIR spectra of NGCNSs pyrolysis. (f) Schematic illustration of the thermal activating process from NGCNSs to DPGCNSs.

leads to the growth of the pore structure.

To elucidate the formation mechanisms of DPGCNSs with high specific surface area, high crystallinity, and enriched defects, the roles of the pyrolysis process are studied. On the one hand, the active-template catalytic pyrolysis temperature greatly affects the role of $FeCl_3{\cdot}6H_2O$ in the graphitization of NGCNSs. When heated at a low temperature (e.g., 600°C), only carbon nanosheets with an amorphous structure are obtained, and the products cannot be transformed into graphitic structures even after a second heating treatment at 1075°C (Fig. S5 in Supplementary Materials). However, excessively high temperature (e.g., 1000°C) can result in a decrease in the total and edge N content in NGCNSs, which prevents the release of N atoms and the formation of carbon defects during subsequent pyrolysis at higher temperatures (Fig. S6 in Supplementary Materials). On the other hand, considering the STA-FTIR results in Fig. 2e, where the intense CO_2 release occurs in the temperature range of approximately 1000–1150°C, the N-removal process of NGCNSs is further conducted at different temperatures to generate control samples (i.e., 1000 and 1150°C; denoted as DPGCNSs-1000 and DPGCNSs-1150, respectively). Notably, as evidenced by the Raman spectra (Fig. S7 in Supplementary Materials), the calculated I_D/I_G first increases from 0.94 (DPGCNSs-1000) to 1.20 (DPGCNSs) and then decreases to 0.80 (DPGCNSs-1150), indicating that DPGCNSs have the highest degree of lattice disorder. The Raman spectra can be further deconvoluted into four peaks, including the G peak (1575 cm^{-1}) corresponding to the graphite-like carbon structure, the D1 peak (1345 cm^{-1}) corresponding to the edge defects of graphitic microcrystals, the D2 peak (1465 cm^{-1}) corresponding to non-six-membered ring topological defects within the plane, and the D3 peak (1185 cm^{-1}) corresponding to defects with sp^3 hybridization[32,33]. Similarly, the peak area ratios of D1 band to G band (I_{D1}/I_G) and D2 band to G band (I_{D2}/I_G) both increased from DPGCNSs-1000 to DPGCNSs-1075, then decreased from DPGCNSs-1075 to DPGCNSs-1150 (Fig. 2a and Fig. S7 in Supplementary Materials). This trend suggests that DPGCNSs synthesized at 1075°C possess the highest concentration of edge and in-plane topological defects, which enhance the adsorption of oxygen species and key intermediates, reduce reaction free energy, and facilitate electron transfer, thereby boosting catalytic activity. These defect types, including topological and edge defects, collectively contribute to superior bifunctional activity by optimizing adsorption and providing active centers[34,35]. A similar variation trend is observed in the pore structure, where S_{BET} first increases from 158 $m^2\ g^{-1}$ (DPGCNSs-1000) to 171 $m^2\ g^{-1}$ (DPGCNSs) and then decreases to 148 $m^2\ g^{-1}$ (DPGCNSs-1150) (Fig. S8 in Supplementary Materials).

These results indicate that the defect sites and pore structure of DPGCNSs undergo a growth and close process at temperatures ranging from 1000 to 1150°C.

Besides heating temperature, the effect of the precursor on the defective structure of the resulting carbon products is also investigated. Similar to polyaniline with –NH– groups as bridges to connect benzene rings, hypercrosslinked polymer (*x*B) with $–CH_2–$ as crosslinking bridges to connect benzene rings (Fig. S9 in Supplementary Materials) is used as a precursor to fabricate GCMs. The as-obtained GCMs are further treated at 1075°C to generate GCMs-1075. Notably, the calculated I_D/I_G of GCMs-1075 (0.30) is lower than that of GCMs (0.34), indicating that GCMs-1075 exhibits a higher degree of graphitization after high-temperature treatment (Fig. S10 in Supplementary Materials). Additionally, the Raman spectra of GCMs reveal that the defect-related D1 and D2 peaks remain low in intensity and essentially unchanged across different pyrolysis temperatures. This indicates that high-temperature treatment alone, in the absence of removable nitrogen dopants, does not generate a significant defect structure. The opposite variation trends in lattice structure, observed between GCMs to GCMs-1075 and NGCNSs to DPGCNSs, clearly demonstrate that the removal of N-doping atoms derived from the molecular precursor generates intrinsic defects in the carbon skeleton.

LSV measurements were recorded in O_2-saturated 0.1 mol L^{-1} KOH electrolyte using a RDE at a scan rate of 10 mV s^{-1} to evaluate the electrocatalytic activity and kinetics of DPGCNSs toward ORR. As shown in Fig. 3a and Fig. S11a in Supplementary Materials, DPGCNSs demonstrate excellent catalytic activity, with an onset potential of 0.916 V and a half-wave potential ($E_{1/2}$) of 0.813 V, which are comparable to those of the Pt/C electrode (0.941 V, $E_{1/2}$ = 0.826 V). To reveal the structural advantage of DPGCNSs, the catalytic performances of NGCNSs, NGCNSs-1000, and NGCNSs-1150 were also evaluated under identical conditions (Fig. S11b–S11d in Supplementary Materials). As shown in Fig. 3a, these samples exhibit significantly lower onset potentials (0.855 V for NGCNSs, 0.898 V for NGCNSs-1000, and 0.856 V for NGCNSs-1150) and half-wave potentials (0.683 V for NGCNSs, 0.801 V for NGCNSs-1000, and 0.748 V for NGCNSs-1150) than those of DPGCNSs. Remarkably, DPGCNSs also exhibit a small Tafel slope of 50.6 mV dec^{-1}, which is lower than those of NGCNSs (65.6 mV dec^{-1}), NGCNSs-1000 (52.5 mV dec^{-1}), NGCNSs-1150 (51.9 mV dec^{-1}), and even the Pt/C catalyst (68.1 mV dec^{-1}) (Fig. 3b), indicating that the enriched defect sites and well-developed porous structure play a crucial role in facilitating ORR kinetics. As shown in Fig. S12 in Supplementary Materials, DPGCNSs exhibit a significantly higher electrochemically active surface area than NGCNSs, demonstrating that defect engineering effectively increases the density of accessible active sites, thereby promoting fast reaction kinetics[36,37]. The hydrogen peroxide (H_2O_2) yield during the ORR process on DPGCNSs was evaluated using RRDE measurements (Fig. S13 in Supplementary Materials). The electron transfer number of DPGCNSs remains above 3.6 over the potential range of 0.2–0.8 V and reaches a maximum value of 3.9 near the half-wave potential. These results indicate a low H_2O_2 yield below 20% for DPGCNSs, suggesting a dominant four-electron transfer pathway for the reduction of O_2 to H_2O. Moreover, compared with the NGCNS catalyst, DPGCNSs exhibit superior long-term stability in O_2-saturated 0.1 mol L^{-1} KOH electrolyte (Fig. S14 in Supplementary Materials).

Similarly, the OER catalytic activity of DPGCNSs was further investigated in O_2-saturated 1 mol L^{-1} KOH electrolyte (Fig. 3c). LSV results demonstrate that a current density of 10 mA cm^{-2} can be achieved for the DPGCNSs at a potential ($E_{j=10}$) of 1.611 V, much lower than those of NGCNSs (1.655 V), DPGCNSs-1000 (1.638 V), DPGCNSs-1150 (1.622 V), and RuO_2 (1.626 V). Also, a Tafel slope of 64.6 mV dec^{-1} is demonstrated for DPGCNSs, much lower

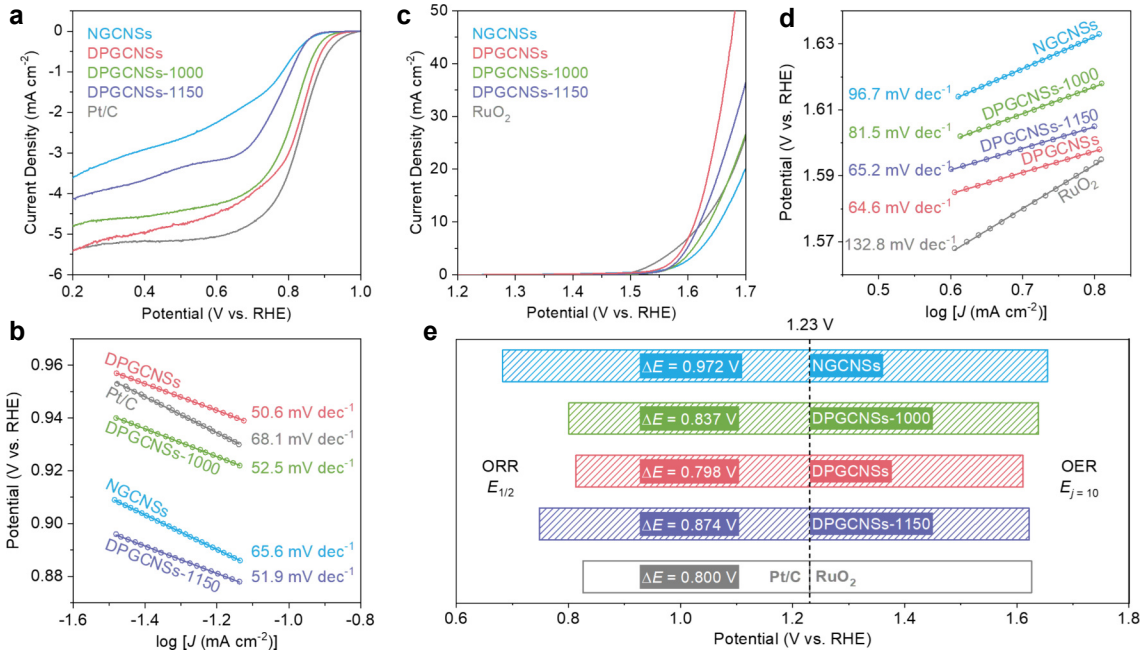

Figure 3 LSV curves in O_2-staurated 0.1 mol L^{-1} KOH solution at 1600 rpm (a) and Tafel plots of different electrocatalysts toward ORR (b). LSV curves (c) and Tafel plots (d) of different electrocatalysts toward OER. (e) Comparison of ΔE for different electrocatalysts.

than those of NGCNSs (96.7 mV dec^{-1}), DPGCNSs-1000 (81.5 mV dec^{-1}), DPGCNSs-1150 (65.2 mV dec^{-1}), and RuO_2 (132.8 mV dec^{-1}) (Fig. 3d). The bifunctional catalytic activity is further revealed by the potential difference of OER and ORR metrics ($\Delta E = E_j = 10 - E_{1/2}$). Notably, DPGCNSs exhibit ΔE of 0.798 V, which is comparable to those of Pt/C and RuO_2 (0.800 V) and significantly lower than those of NGCNSs (0.972 V), DPGCNSs-1000 (0.837 V), and DPGCNSs-1150 (0.874 V) (Fig. 3e). The overall performance of DPGCNSs is competitive with that of recently reported metal-free carbon-based bifunctional catalysts, highlighting the effectiveness of defect engineering via nitrogen removal in enhancing catalytic activity (Fig. S15 and Table S2 in Supplementary Materials)[23,38–45]. Moreover, when the I_D/I_G from the Raman measurement is connected with the ORR and OER activity, it can be found that the highest I_D/I_G corresponds to the best ORR and OER kinetics, strongly confirming that defective and porous structures enable promoted electrocatalytic performances. It should be noted that the values of I_{D1}/I_G and I_{D2}/I_G are positively correlated with the ORR and OER catalytic activity, strongly confirming that defective and porous structures promote electrocatalytic performances[32]. In contrast, all GCM samples treated at different temperatures demonstrate consistently poor catalytic activity (Figs. S16 and S17 in Supplementary Materials). The GCMs showed a low $E_{1/2}$ (0.727 V) for ORR and minimal OER catalytic ability with a current density of only 1.6 mA cm^{-2} at 1.7 V. Moreover, no significant improvement in ORR or OER performance was observed with increasing pyrolysis temperature. Even after treatment at 1075°C, the GCMs-1075 reached only an $E_{1/2}$ of 0.733 V and an OER current density of 4.2 mA cm^{-2} at 1.7 V, which are far inferior to those of defect-rich DPGCNSs. This limited and temperature-insensitive catalytic activity can be directly attributed to the absence of an effective defect-generation mechanism within the carbon framework during synthesis.

Considering the superior bifunctional ORR and OER catalytic activity of DPGCNSs, primary Zn–air batteries are assembled with DPGCNSs as the air cathode catalyst. As shown in Fig. 4a, a light-emitting diode array panel can be lightened up by two series DPGCNSs catalyst-loaded Zn–air batteries. The Zn–air battery with DPGCNSs catalyst delivers a peak power density of 55 mW cm^{-2}, significantly larger than that with Pt/C+RuO_2 catalysts (44 mW cm^{-2}) (Fig. 4b). Additionally, the battery with DPGCNSs catalyst can achieve a specific capacity of up to 780 mA h g_{Zn}^{-1} at 2 mA cm^{-2}, corresponding to 94% of the theoretical capacity (830 mA h g_{Zn}^{-1}), much higher than with Pt/C+RuO_2 catalysts (692 mA h g_{Zn}^{-1}) (Fig. 4c). More importantly, the battery with the DPGCNSs catalyst exhibits significantly smaller voltage drops during galvanostatic discharge at high current densities, indicating accelerated reaction kinetics (Fig. 4d). Rechargeable Zn–air batteries were further evaluated by galvanostatic charge–discharge cycling at a current density of 2 mA cm^{-2}. Notably, the voltage gap of the battery employing the DPGCNSs catalyst decreases from 0.97 V at the initial cycles to 0.72 V after 400 h of cycling, which is markedly superior to that of the Pt/C+RuO_2-based battery, whose voltage gap increases from 0.72 V at the initial cycles to 1.38 V after 400 h of cycling. Moreover, the DPGCNSs-based battery maintains stable operation without obvious voltage fading over 700 cycles, demonstrating the strong potential of DPGCNSs for application in rechargeable

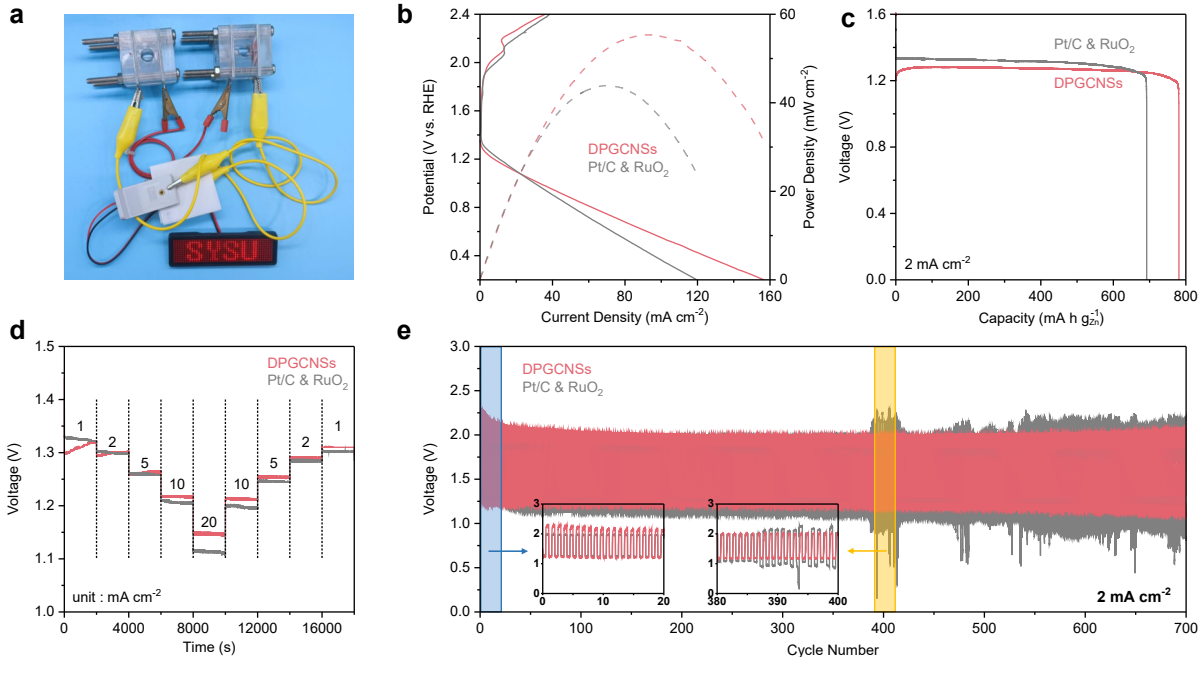

Figure 4 (a) Digital photo of an LED panel lightened by two Zn–air batteries with DPGCNSs catalyst. (b) Discharge curves and the corresponding power densities of Zn–air batteries with DPGCNSs and Pt/C+RuO_2 catalysts. (c) Galvanostatic discharge curves of Zn–air batteries with DPGCNSs and Pt/C+RuO_2 catalysts at 2 mA cm^{-2}. The specific capacity is normalized based on the mass of the consumed Zn anode. Discharge profiles at different current densities (d) and long-term cycling tests at 2 mA cm^{-2} (e) of the rechargeable Zn–air batteries loaded with DPGCNSs and Pt/C+RuO_2.

Zn–air batteries.

4 Conclusion

In summary, graphitic carbon nanosheets enriched with intrinsic defects and high surface area were successfully fabricated via nitrogen atom removal defect engineering for efficient oxygen electrocatalysis. It was demonstrated that thermally driven elimination of nitrogen atoms induces the rearrangement of neighboring carbon atoms, generating abundant carbon defects and increasing the surface area while preserving the long-range ordered graphitic structure. As a result, the as-constructed DPGCNSs uniquely integrate abundant intrinsic defects with high electrocatalytic activity, a highly graphitic skeleton with excellent electrical conductivity, and a two-dimensional porous architecture that enables rapid mass transport. Consequently, DPGCNSs exhibit outstanding bifunctional electrocatalytic performance toward ORR and OER, characterized by low overpotentials, favorable reaction kinetics, and excellent long-term stability in rechargeable Zn–air batteries. These findings provide valuable insights into the rational design and scalable fabrication of high-performance graphitic carbon-based electrocatalysts, and are expected to promote their broader application in renewable and clean energy conversion systems.

Acknowledgements

None.

Author contribution statement

Y. Chen, J. Huang and S. Liu are responsible for conceptualization. M. Liu and S. Liu supervised the project. Y. Chen, Z. Cen and J. Huang designed the experiments. Y. Chen and Z. Cen synthesized materials and characterized the structure and basic properties. Y. Tan, M. Liang and Y. Ji assisted in structure characterizations. Y. Chen, Z. Cen, J. Huang, M. Liu and S. Liu contributed to the preparation of this manuscript. All the authors have approved the final manuscript.

Data availability

The data that supports the findings of this study is available from the corresponding author upon reasonable request.

Declaration of competing interest

All the contributing authors report no conflicts of interest in this work.

Funding

This work is granted by the National Key Research and Development Program of China (Grant Nos. 2021YFF0500600 and 2021YFA1202802), the National Natural Science Foundation of China (Grant Nos. 52472058, 22479087 and 52203298), Guangdong Province Foundation for Distinguished Young Scholars (Grant Nos. 2024B1515020092 and 2024B1515020023), Guangdong Innovative and Entrepreneurial Research Team Program (Grant No. 2023ZT10L039), Shenzhen Science and Technology Program (Grant No. KQTD20240729102048053).

Use of AI statement

None.

Electronic Supplementary Material: Supplementary material is available in the online version of this article at https://doi.org/10.26599/EMD.2026.9370084

References

[1] Wang, Z., Jin, X. Y., Zhu, C., Liu, Y. P., Tan, H., Ku, R., Zhang, Y. Q., Zhou, L. J., Liu, Z., Hwang, S. J., et al. (2021). Atomically dispersed Co_2-N_6 and Fe-N_4 costructures boost oxygen reduction reaction in both alkaline and acidic media. *Adv. Mater.* 33, 2104718.

[2] Lin, Y. Y., Zhu, Y. L., Ma, Q., Ke, X. L., Ma, P. W., Liao, R. F., Liu, S. H., Wu, D. C. (2022). Self-supporting electrocatalyst film based on self-assembly of heterogeneous bottlebrush and polyoxometalate for efficient hydrogen evolution reaction. *Macromol. Rapid Commun.* 43, 2100915.

[3] Yan, D. F., Li, Y. X., Huo, J., Chen, R., Dai, L. M., Wang, S. Y. (2017). Defect chemistry of nonprecious-metal electrocatalysts for oxygen reactions. *Adv. Mater.* 29, 1606459.

[4] Vinayan, B. P., Nagar, R., Rajalakshmi, N., Ramaprabhu, S. (2012). Novel platinum–cobalt alloy nanoparticles dispersed on nitrogen-doped graphene as a cathode electrocatalyst for PEMFC applications. *Adv. Funct. Mater.* 22, 3519–3526.

[5] Feng, Q. C., Zhao, S., Xu, Q., Chen, W. X., Tian, S. B., Wang, Y., Yan, W. S., Luo, J., Wang, D. S., Li, Y. D. (2019). Mesoporous nitrogen-doped carbon-nanosphere-supported isolated single-atom Pd catalyst for highly efficient semihydrogenation of acetylene. *Adv. Mater.* 31, 1901024.

[6] Mirshokraee, S. A., Muhyuddin, M., Lorenzi, R., Tseberlidis, G., Vecchio, C. L., Baglio, V., Berretti, E., Lavacchi, A., Santoro, C. (2023). Litchi-derived platinum group metal-free electrocatalysts for oxygen reduction reaction and hydrogen evolution reaction in alkaline media. *SusMat* 3, 248–262.

[7] Wang, H., Shao, Y., Mei, S. L., Lu, Y., Zhang, M., Sun, J. K., Matyjaszewski, K., Antonietti, M., Yuan, J. Y. (2020). Polymer-derived heteroatom-doped porous carbon materials. *Chem. Rev.* 120, 9363–9419.

[8] Su, D. S., Perathoner, S., Centi, G. (2013). Nanocarbons for the development of advanced catalysts. *Chem. Rev.* 113, 5782–5816.

[9] Gottlieb, E., Matyjaszewski, K., Kowalewski, T. (2019). Polymer-based synthetic routes to carbon-based metal-free catalysts. *Adv. Mater.* 31, 1804626.

[10] Lu, Y. H., Tang, Y. C., Liu, R. L., Li, C. F., Liu, S. H., Zhu, Y. L., Wu, D. C. (2022). Multifunctional templating strategy for fabrication of Fe, N-codoped hierarchical porous carbon nanosheets. *Chin. J. Polym. Sci.* 40, 2–6.

[11] Meng, J., Liu, H. D., Xu, J. N., Lou, Y. H., Sun, H. X., Jiang, B., Liu, Y. Z., Qin, H. F., Dou, S., Yu, H. P. (2024). Nanocarbon catalysts with co-active S−P−C sites enhance metal-free direct oxidation of alcohols. *SusMat* 4, e221.

[12] Han, A. L., Zhang, Z. D., Yang, J. R., Wang, D. S., Li, Y. D. (2021). Carbon-supported single-atom catalysts for formic acid oxidation and oxygen reduction reactions. *Small* 17, 2004500.

[13] Yang, Y. C., Yang, Y. W., Pei, Z. X., Wu, K. H., Tan, C. H., Wang, H. Z., Wei, L., Mahmood, A., Yan, C., Dong, J. C., et al. (2020). Recent progress of carbon-supported single-atom catalysts for energy conversion and storage. *Matter* 3, 1442–1476.

[14] Xie, X. H., He, C., Li, B. Y., He, Y. H., Cullen, D. A., Wegener, E. C., Kropf, A. J., Martinez, U., Cheng, Y. W., Engelhard, M. H., et al. (2020). Performance enhancement and degradation mechanism identification of a single-atom Co–N–C catalyst for proton exchange membrane fuel cells. *Nat. Catal.* 3, 1044–1054.

[15] Zhang, J. Q., Zhao, Y. F., Chen, C., Huang, Y. C., Dong, C. L.,

清華大學出版社 Tsinghua University Press | SciOpen

Chen, C. J., Liu, R. S., Wang, C. Y., Yan, K., Li, Y. D., et al. (2019). Tuning the coordination environment in single-atom catalysts to achieve highly efficient oxygen reduction reactions. *J. Am. Chem. Soc.* 141, 20118–20126.

[16] Herold, F., Prosch, S., Oefner, N., Brunnengräber, K., Leubner, O., Hermans, Y., Hofmann, K., Drochner, A., Hofmann, J. P., Qi, W., et al. (2021). Nanoscale hybrid amorphous/graphitic carbon as key towards next-generation carbon-based oxidative dehydrogenation catalysts. *Angew. Chem. Int. Ed.* 60, 5898–5906.

[17] Wang, H. P., Li, X. B., Gao, L., Wu, H. L., Yang, J., Cai, L., Ma, T. B., Tung, C. H., Wu, L. Z., Yu, G. (2018). Three-dimensional graphene networks with abundant sharp edge sites for efficient electrocatalytic hydrogen evolution. *Angew. Chem. Int. Ed.* 57, 192–197.

[18] Xia, D. S., Tang, F., Yao, X. Z., Wei, Y. P., Cui, Y. F., Dou, M., Gan, L., Kang, F. Y. (2020). Seeded growth of branched iron–nitrogen-doped carbon nanotubes as a high performance and durable non-precious fuel cell cathode. *Carbon* 162, 300–307.

[19] Li, S., Cheng, C., Liang, H. W., Feng, X. L., Thomas, A. (2017). 2D porous carbons prepared from layered organic-inorganic hybrids and their use as oxygen-reduction electrocatalysts. *Adv. Mater.* 29, 1700707.

[20] Yang, H. Z., Huang, J. L., Liu, S. H., Chen, Y. Q., Cen, Z. H., Shi, C. G., Lu, Y. H., Fu, R. W. (2023). Pseudocapacitive potassium-ion intercalation enabled by topologically defective soft carbon toward high-rate, large-areal-capacity, and low-temperature potassium-ion batteries. *Small* 19, 2302537.

[21] Dong, Y., Zhang, Q. J., Tian, Z. Q., Li, B. R., Yan, W. S., Wang, S., Jiang, K. M., Su, J. W., Oloman, C. W., Gyenge, E. L., et al. (2020). Ammonia thermal treatment toward topological defects in porous carbon for enhanced carbon dioxide electroreduction. *Adv. Mater.* 32, 2001300.

[22] Yi, T., Huang, J. L., Cen, Z. H., Ji, Y. W., Liu, S. H. (2024). N/S co-doped carbon nanosheets for the efficient electrochemical extraction of uranium from seawater. *New Carbon Mater.* 39, 1108–1116.

[23] Chen, Y. Q., Huang, J. L., Chen, Z. R., Shi, C. G., Yang, H. Z., Tang, Y. C., Cen, Z. H., Liu, S. H., Fu, R. W., Wu, D. C. (2022). Molecular engineering toward high-crystallinity yet high-surface-area porous carbon nanosheets for enhanced electrocatalytic oxygen reduction. *Adv. Sci.* 9, 2103477.

[24] Jia, Y., Zhang, L. Z., Du, A. J., Gao, G. P., Chen, J., Yan, X. C., Brown, C. L., Yao, X. D. (2016). Defect graphene as a trifunctional catalyst for electrochemical reactions. *Adv. Mater.* 28, 9532–9538.

[25] Wang, X., Jia, Y., Mao, X., Zhang, L. Z., Liu, D. B., Song, L., Yan, X. C., Chen, J., Yang, D. J., Zhou, J. Z., et al. (2020). A directional synthesis for topological defect in carbon. *Chem* 6, 2009–2023.

[26] Gan, G. Q., Fan, S. Y., Li, X. Y., Wang, J., Bai, C. P., Guo, X. C., Tade, M., Liu, S. M. (2021). Nature of intrinsic defects in carbon materials for electrochemical dechlorination of 1,2-dichloroethane to ethylene. *ACS Catal.* 11, 14284–14292.

[27] Jaouen, F., Charreteur, F., Dodelet, J. P. (2006). Fe-based catalysts for oxygen reduction in PEMFCs: importance of the disordered phase of the carbon support. *J. Electrochem. Soc.* 153, A689.

[28] Zhu, J. W., Huang, Y. P., Mei, W. C., Zhao, C. Y., Zhang, C. T., Zhang, J., Amiinu, I. S., Mu, S. C. (2019). Effects of intrinsic pentagon defects on electrochemical reactivity of carbon nanomaterials. *Angew. Chem. Int. Ed.* 58, 3859–3864.

[29] Ni, W. P., Liu, Z. X., Zhang, Y., Ma, C., Deng, H. Q., Zhang, S. G., Wang, S. Y. (2021). Electroreduction of carbon dioxide driven by the intrinsic defects in the carbon plane of a single Fe-N_4 site. *Adv. Mater.* 33, 2003238.

[30] Gao, Y. F., Liang, S., Liu, B. M., Jiang, C. X., Xu, C. Y., Zhang, X. Y., Liang, P., Elimelech, M., Huang, X. (2023). Subtle tuning of nanodefects actuates highly efficient electrocatalytic oxidation. *Nat. Commun.* 14, 2059.

[31] Chen, Y. X., Xi, B. J., Huang, M., Shi, L. L., Huang, S. Z., Guo, N. N., Li, D., Ju, Z. C., Xiong, S. L. (2022). Defect-selectivity and "Order-in-Disorder" engineering in carbon for durable and fast potassium storage. *Adv. Mater.* 34, 2108621.

[32] Lai, Q. X., Zheng, J., Tang, Z. M., Bi, D., Zhao, J. X., Liang, Y. Y. (2020). Optimal configuration of N-doped carbon defects in 2D turbostratic carbon nanomesh for advanced oxygen reduction electrocatalysis. *Angew. Chem. Int. Ed.* 59, 11999–12006.

[33] Huang, J. L., Chen, Y. Q., Cen, Z. H., Yi, T., Liang, M., Zhu, Y. L., Liu, R. L., Fu, R. W., Liu, S. H., Wu, D. C. (2024). Topological defect-regulated porous carbon anodes with fast interfacial and bulk kinetics for high-rate and high-energy-density potassium-ion batteries. *Adv. Mater.* 36, 2403033.

[34] Bhatt, M. D., Kim, H., Kim, G. (2022). Various defects in graphene: a review. *RSC Adv.* 12, 21520–21547.

[35] Yan, X. C., Jia, Y., Odedairo, T., Zhao, X. J., Jin, Z., Zhu, Z. H., Yao, X. D. (2016). Activated carbon becomes active for oxygen reduction and hydrogen evolution reactions. *Chem. Commun.* 52, 8156–8159.

[36] Lv, J. J., Li, Y. L., Wu, S. J., Fang, H., Li, L. L., Song, R. B., Ma, J., Zhu, J. J. (2018). Oxygen species on nitrogen-doped carbon nanosheets as efficient active sites for multiple electrocatalysis. *ACS Appl. Mater. Interfaces* 10, 11678–11688.

[37] Han, X. P., Ling, X. F., Wang, Y., Ma, T. Y., Zhong, C., Hu, W. B., Deng, Y. D. (2019). Generation of nanoparticle, atomic-cluster, and single-atom cobalt catalysts from zeolitic imidazole frameworks by spatial isolation and their use in zinc–air batteries. *Angew. Chem. Int. Ed.* 58, 5359–5364.

[38] Liu, C., Liu, F., Li, H., Chen, J. S., Fei, J. Y., Yu, Z. X., Yuan, Z. W., Wang, C. J., Zheng, H. L., Liu, Z. W., et al. (2021). One-dimensional van der Waals heterostructures as efficient metal-free oxygen electrocatalysts. *ACS Nano* 15, 3309–3319.

[39] Xiao, X., Li, X. H., Wang, Z. X., Yan, G. C., Guo, H. J., Hu, Q. Y., Li, L. J., Liu, Y., Wang, J. X. (2020). Robust template-activator cooperated pyrolysis enabling hierarchically porous honeycombed defective carbon as highly-efficient metal-free bifunctional electrocatalyst for Zn-air batteries. *Appl. Catal. B: Environ.* 265, 118603.

[40] Murugesan, C., Senthilkumar, B., Barpanda, P. (2022). Biowaste-derived highly porous N-doped carbon as a low-cost bifunctional electrocatalyst for hybrid sodium–air batteries. *ACS Sustainable Chem. Eng.* 10, 9077–9086.

[41] Kong, F. T., Qiao, Y., Zhang, C. Q., Fan, X. H., Zhao, Q. B., Kong, A. G., Shan, Y. K. (2020). Oriented synthesis of pyridinic-n dopant within the highly efficient multifunction carbon-based materials for oxygen transformation and energy storage. *ACS Sustainable Chem. Eng.* 8, 10431–10443.

[42] Lei, H., Cui, M. W., Huang, Y. (2022). S-doping promotes pyridine nitrogen conversion and lattice defects of carbon nitride to enhance the performance of Zn–Air batteries. *ACS Appl. Mater. Interfaces* 14, 34793–34801.

[43] Guo, Y. B., Yao, S., Gao, L. X., Chen, A., Jiao, M. G., Cui, H. J., Zhou, Z. (2020). Boosting bifunctional electrocatalytic activity in S and N co-doped carbon nanosheets for high-efficiency Zn–air batteries. *J. Mater. Chem. A* 8, 4386–4395.

[44] Wu, Z. H., Yu, Y. R., Zhang, G. K., Zhang, Y. S., Guo, R. X., Li, L., Zhao, Y. G., Wang, Z., Shen, Y. L., Shao, G. S. (2022). In situ monitored (N, O)-doping of flexible vertical graphene films with high-flux plasma enhanced chemical vapor deposition for remarkable metal-free redox catalysis essential to alkaline zinc–air batteries. *Adv. Sci.* 9, 2200614.

[45] Lu, T. T., Hu, X. L., He, J. J., Li, R., Gao, J., Lv, Q., Yang, Z., Cui, S., Huang, C. S. (2021). Aqueous/solid state Zn-air batteries based on N doped graphdiyne as efficient metal-free bifunctional catalyst. *Nano Energy* 85, 106024.

Open Access This article is licensed under a Creative Commons Attribution 4.0 International License (CC BY 4.0), which permits reusers to distribute, remix, adapt, and build upon the material in any medium or format, so long as attribution is given to the original author(s) and the source, a link to the license is provided, and any changes made are indicated. See https://creativecommons.org/licenses/by/4.0/

© The author(s) 2026. Published by Tsinghua University Press.